# Separating convective from diffusive mass transport mechanisms in ionic liquids by redox pro-fluorescence microscopy

Mattia Belotti,[a] Mohsen M. T. El-Tahawy,[b,c] Marco Garavelli,[b] Michelle L. Coote,[d] K. Swaminathan Iyer,[e] and Simone Ciampi*[,a]

[a] School of Molecular and Life Sciences, Curtin University, Bentley, Western Australia 6102, Australia; Email: simone.ciampi@curtin.edu.au

[b] Dipartimento di Chimica Industriale "Toso Montanari", Università di Bologna, Bologna, Emilia Romagna, 40136, Italy

[c] Chemistry Department, Faculty of Science, Damanhour University, Damanhour 22511, Egypt

[d] Institute for Nanoscale Science and Technology, College of Science and Engineering, Flinders University Bedford Park, South Australia, 5042, Australia

[e] School of Molecular Sciences, The University of Western Australia, Perth, Western Australia 6009, Australia

**ABSTRACT.** The study of electrochemical reactivity requires analytical techniques capable of probing the diffusion of reactants and products to and from electrified interfaces. Information on diffusion coefficients are often obtained indirectly by modelling current transients and cyclic voltammetry data, but such measurements lack spatial resolution and are accurate only if mass transport by convection is negligible. Detecting and accounting for adventitious convection in viscous and wet solvents, such as ionic liquids, is technically challenging. We have developed a direct, spatiotemporally resolved optical tracking of diffusion fronts which can detect and resolve convective disturbances to linear diffusion. By tracking the movement of an electrode-generated fluorophore we demonstrate that parasitic gas evolving reactions lead to ten-fold overestimates of macroscopic diffusion coefficients. An hypothesis is put forward linking large barriers to inner-sphere redox reactions, such as hydrogen gas evolution, to the formation of cation-rich overscreening and crowding double layer structures in imidazolium-based ionic liquids.

## INTRODUCTION

Room temperature ionic liquids (RTILs) are salts with melting point below 25 °C.[1] They are non-volatile ionic conductors, with emerging applications in technologies and processes ranging from batteries,[2] to supercapacitors,[3] electrocatalysis,[4] and sensing.[5, 6] For all RTIL-based electrochemical applications it is important to first obtain a correct and complete understanding of mass transport of reactants and products towards and away from the electrode.[7-9] Equally important is to access quantitative information on structures and dynamics of the electrode–RTIL interface.[10-14] For instance, insights on double layer order obtained by atomic force microscopy (AFM),[15, 16] Raman spectroscopy,[17] and more recently even through simple measurements of open circuit potential,[13] have shown the existence of compact cation or anion-rich layers near polarized electrodes.[13] It can be supposed that such highly ordered and compact RTIL arrangements, which can persist for several hours if formed in response to negative electrode biases,[13] will introduce a kinetic limitation to heterogeneous charge-transfer reactions, especially for reactions highly dependent on the nature of the electrode interface, such as inner-sphere reduction of water, oxygen or protons.[18, 19] Opposite to outer-sphere reactions, which proceed at appreciable rates even when there exist a solvent layer between electrode and reactant, inner-sphere reactions require a strong interaction between electrode's surface and molecule being oxidized or reduced.[18, 20, 21]

Hence a near-surface compact arrangement of large organic cations is likely introduce a barrier to a common unwanted inner-sphere reaction: evolution of hydrogen as bubbles.[18, 22] Parasitic evolution of gas bubbles at electrodes is a common occurrance,[23-26] and partial masking of the electrode's surface by a gas cavity can decrease its capacitance,[27] or cause an increase in electrical conductivity during electrolysis.[28-30] Beside the loss of electroactive area, a convective contribution to mass transport will appear as the surface-pinned bubble grows and eventually departs the electrode.[31] Such bubble-induced "disturbance" to diffusion – a localized and transient stirring – is often neglected and/or hard to account for.[32] In this work we seek to develop a simple tool to quantify, and to map across a macroscopic electrode, the impact of adventitious gas evolution reactions on the analysis of mass transport in RTILs. The study of reactant and product diffusivity is a central feature of most electrochemical investigations,[33, 34] but in conventional "one-electrode, one-lead"[35] measurement, local information on convection disturbances to quiescent diffusion are inevitably lost.[36-38]

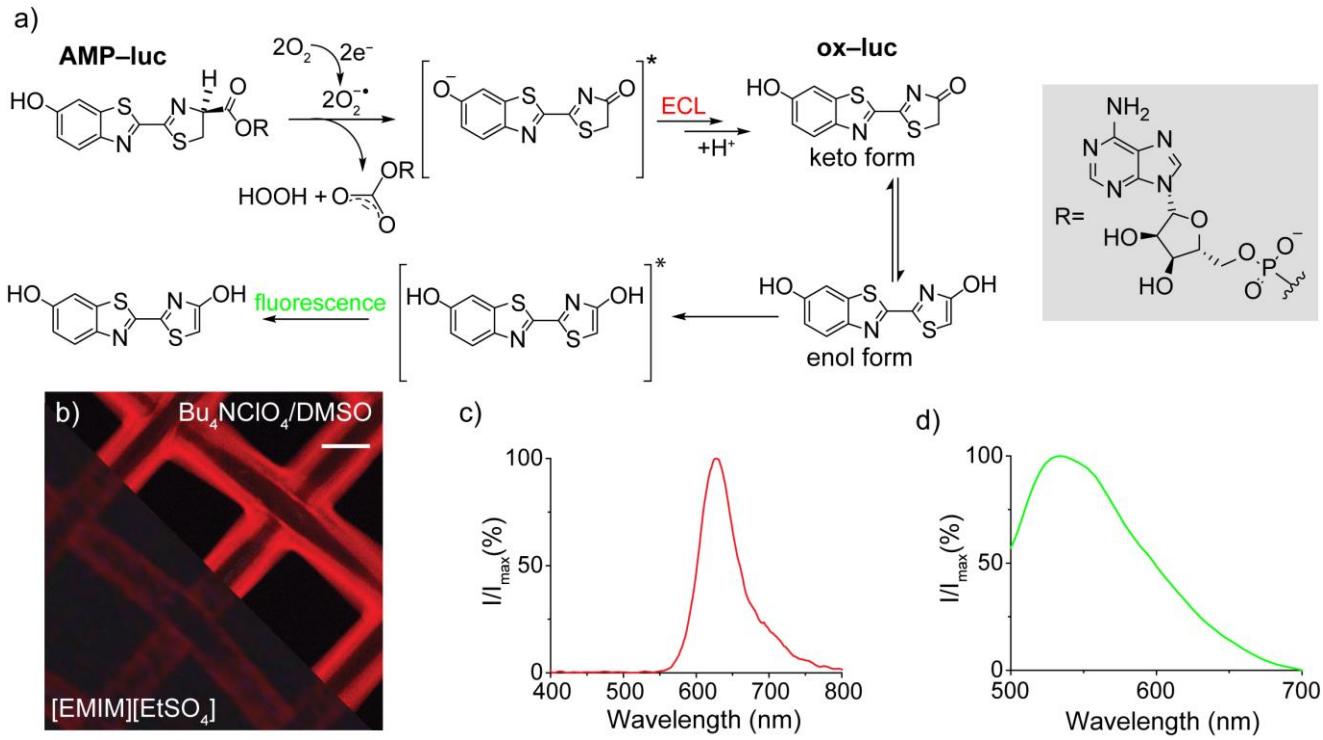


**Figure 1.** (a) Proposed mechanism for the cathodic electrochemiluminescence (ECL) of **AMP–luc**.[39] (b) The reaction of **AMP–luc** ($0.4 \times 10^{-3}$ M, oxygen-saturated, −2.0 V vs Ag/AgCl) with electrode-generated superoxide leads to the excited state of **ox–luc**, which relaxes emitting red light. The red ECL emission is intense for electrolyses in $2.0 \times 10^{-1}$ M $Bu_4NClO_4$/DMSO (10× magnification, CMOS sensor camera, unmodified micrograph, Video S1) but very faint in [EMIM][$EtSO_4$] (Laowa 25 mm F/2.8 2.5−5X, back-illuminated CMOS sensor, micrographs edited to maximise contrast). The scale bar is 100 µm. (c) Cathodic **AMP–luc** ECL spectrum recorded in [EMIM][$EtSO_4$]. (d) Optical excitation of an electrolyzed **AMP–luc**/[EMIM][$EtSO_4$] triggers the green fluorescence of the **ox–luc** enol product.

In the 1990s Engstrom and co-workers began developing fluorescence microscopy-based approaches to access two-dimensional information on concentration gradients across macroscopic electrodes.[40-42] The same group also applied electrochemiluminescent (ECL) reactions to map current heterogeneity due to non-uniform diffusion at the edge of microelectrodes,[43-45] demonstrating the electroanalytical value of optical techniques.[46-48] Other groups have since then explored similar research lines, and have for example by developing electrofluorochromic redox couples to monitor the evolution over time of electrode concentration profiles and pH gradients.[49-55]

In this paper we develop a strategy for the visualization of diffusion fronts by means of tracking the movement of electrochemically generated fluorophores. Such spatiotemporally resolved data on diffusion coefficients allowed us to detect and quantify bubble-induced convective disturbances of nominally quiescent electrode systems. We have applied this optical approach – redox profluorescence microscopy – to RTILs that have a different propensity of forming compact double layer cation-rich structures, hence a different intrinsic inhibition of adventitious inner-sphere gas-evolving redox reactions. The electrode-generated fluorophore is oxyluciferin (**ox–luc**, Figure 1a),[56] which is the final product of the cathodic electrochemiluminescent (ECL, Figure 1b and Video S1, Supporting Information) light-path of non-fluorescent firefly's luciferin adenylate ester (**AMP–luc**).[39]

## EXPERIMENAL SECTION

**Materials.** Unless stated otherwise, all reagents were of analytical grade and used without further purification. Milli-Q™ water (> 18.2 MΩ cm) was used for cleaning procedures and, where specified, for adjusting the water content of the RTIL samples. D-luciferin sodium salt (≥95%, Cayman Chemical Company, Michigan) was used as starting material for the synthesis of firefly luciferyl adenylate (hereafter **AMP–luc**). **AMP–luc** was prepared and titrated as described previously.[39, 57] Pyridine (≥99.5%) and acetonitrile (≥99.9%, MeCN) were purchased from Honeywell (North Carolina). 1-Butyl-1-methylpyrrolidinium bis-(trifluoromethylsulfonyl)imide (99.5%, [BMPyrr][$NTf_2$]), 1-ethyl-3-methylimidazolium tetrafluoroborate (>98%, [EMIM][$BF_4$]) were purchased from Iolitec (Germany). Adenosine 5'-monophosphate monohydrate (≥97%, AMP), *N*,*N*'-dicyclohexylcarbodiimide (99%,), 1-ethyl-3-methylimidazolium ethyl sulfate (≥95%, [EMIM][$EtSO_4$]), tetrabutylammonium hexafluorophosphate (≥99.0%, $Bu_4NPF_6$), bis(cyclopentadienylcobalt(III) hexafluorophosphate (98%, $Cc^+$), bis(pentamethylcyclopentadienyl)cobalt(III) hexafluorophosphate (98%, $Me_{10}Cc^+$), potassium dioxide ($KO_2$, ≥95%), and ferrocene (98%, Fc, sublimed before use) were purchased from Sigma. The water content in RTIL samples was estimated by Karl-Fisher (KF) titrations using a C20S compact KF coulometer (Mettler–Toledo, Ohio). Hydranal™ Coulomat AG reagent for the KF titration was purchased from Honeywell

(North Carolina), and the 0.1% water standard was from Merck (Germany). At least three KF titrations were performed for each RTIL. The reported values ([EMIM][$EtSO_4$], 930 ppm; [BMPyrr][$NTf_2$], 125 ppm; [EMIM][$BF_4$], 2400 ppm) are the arithmetic average of the three titrations.

**Fluorescence and ECL imaging.** Unless specified otherwise, time-resolved fluorescence and ECL images were recorded on a Nikon ECLIPSE Ti2-U inverted microscope fitted with a custom-built optoelectrochemical single-compartment, three-electrode cell (Figure S1, Supporting Information). Microscopy experiments were performed in a dark room, at room temperature (23 ± 2 °C) in air, and within 10 min of exposing the electrolytic **AMP–luc** solution to the atmosphere. For the fluorescence experiments the microscope was fitted with a Plan Apo λ 10×/0.45 objective (part n. 88-379, Nikon, CFI Plan Fluor), a back-illuminated CMOS monochrome camera (DS-Qi2, Nikon), and a FITC filter/dichroic mirror cube (LED-FITC-A-NTF-ZERO, single band excitation filter 461.0–487.5 nm, single band emission filter 502.5–547.5 nm, and 495 nm dichroic beamsplitter, BrightLine®, Semrock, California). Fluorescence videos were recorded selecting a 20 ms exposure time, a capture rate of 5 frame/s, and a 1× gain. Microscopy experiments to map ECL in organic solvents (**AMP–luc** in $Bu_4NClO_4$/DMSO, e.g. video frame in Figure 1b, upper right section) were recorded using a colour camera (DS-Fi3, Nikon), setting the exposure to 1.0 s, and without filtering nor light excitation. ECL intensities for solutions of **AMP–luc** in RTILs were however to dim to be captured with the DS-Fi3 camera, so that ECL images (e.g. lower left section of Figure 1b, cathodic electrolysis of **AMP–luc** in [EMIM][$EtSO_4$]) were recorded with a more sensitive DSLR camera (Nikon D850) equipped with back-illuminated CMOS image sensor and using an ultra macro lens (Laowa 25 mm F/2.8 2.5–5X). The fluorescence of non-fluorescent **AMP–luc** solutions ($0.4 \times 10^{-3}$ M, ~10 mL) was triggered electrochemically by applying a short (30 s) cathodic bias (−2.0 V vs reference electrode) to a platinum mesh working electrode (SEC-C Gauze, 80 mesh, 80 µm wire diameter, 7 × 6 mm outer size, purchased from BASi, Indiana). The reference electrode was a plastic body "leakless" Ag/AgCl electrode (eDAQ, part n. ET072-1, with 3.4 M aqueous potassium chloride as filling solution) and a platinum coil served as the counter electrode (0.5 mm diameter wire, 99.99+%, Goodfellow Cambridge Limited). The electrodes were connected to a portable potentiostat (Emstat3 blue, PalmSens BV, Netherlands). The **AMP–luc** solutions were bubbled with oxygen gas (≥99.95%, Coregas) for at least 20 min prior to the experiments. The platinum electrodes were cleaned daily through at least 50 consecutive cyclic voltammetry cycles (from −2.0 V to 1.0 V, potential scan rate of 0.01 V $s^{-1}$) in $5.0 \times 10^{-1}$ M aqueous sulphuric acid. Local diffusivity values were calculated by analyzing the movement of the **ox–luc** fluorescent front away from the platinum surface. Time-stamped fluorescence intensity profiles were analysed with the open source image processing package Fiji,[58] in order to determine the distance ($r$) from the electrode surface at which the fluorescence intensity falls to half of its maximum value. This distance ($r$) was tracked as function of the time ($t$) after the cathodic pulse, and used to estimate diffusion coefficients ($D$) by assuming an Einstein's random walk ($r^2 = 2Dt$).[59, 60] This procedure was repeated for 10 different videos for each RTIL type, with at least 10 different locations analyzed in each video. Fluorescence images were not background subtracted, and no attempts were made to improve contrast and sharpness. ECL images for RTIL samples were background-subtracted.

**Photon counting.** A single-photon counting module (SPCM-AQR-14, Excelitas Technologies), interfaced with an avalanche photodiode (APD) controller (Nanonics Imaging Ltd. time constant was set to 1.0 ms), was used to perform quantitative ECL measurements. A data logger (DrDAQ, Pico Technology) was used to record photon count rates. Electrolytic **AMP–luc** solutions and the three electrodes described for the fluorescence imaging experiments were placed inside a quart cuvette (10 mm optical path, Starna Pty Ltd., Australia). The cuvette was fitted with a custom PTFE cap/electrode holder to ensure reproducible electrodes positioning.

**Fluorescence and ECL spectroscopy.** ECL and fluorescence spectra were recorded on a Cary Eclipse (Varian, California) fluorescence spectrophotometer operated either in Bio/Chemi-luminescence mode (ECL, no excitation) or in Fluorescence mode (474 nm, excitation). The experiments were performed using the cuvette described in the Photon counting section, and the electrodes are described in the Fluorescence and ECL imaging section.The spectrometer's photomultiplier voltage was set to 800 V and the emission slit to 20 nm for both ECL and fluorescence measurements. The fluorescence excitation slit was set to 20 nm.

**Open circuit potentiometry.** Time-resolved open circuit potential (OCP) measurements were performed with a Emstat3 Blue potentiostat (PalmSens BV, Netherlands). A small RTIL sample (~5 mL) was loaded in a 10 mL beaker and degassed by means of bubbling argon gas (99.997%, Coregas) through it for at least 20 min. A platinum mesh (SEC-C Gauze, 80 mesh, BASi, Indiana) was used as working electrode, a platinum coil as counter electrode, and an Ag/AgCl "leakless" as the reference electrode (eDAQ, part ET072-1). The reference electrode potential was calibrated against the apparent formal potential of the ferrocene/ferricenium couple ($Fc/Fc^+$) as measured by cyclic voltammetry at a platinum disk electrode (eDAQ, ET052, 3 mm diameter) using the above specified reference and counter electrodes and a $1.0 \times 10^{-3}$ M ferrocene solution in $1.0 \times 10^{-1}$ M $Bu_4NClO_4$/MeCN. The working electrode was polished with alumina slurry (0.05 µm, eDAQ, ET033) and then cleaned electrochemically as described in the Fluorescence Imaging section. The OCP measurements were started immediately after a 60 s cathodic pulse (−2.0 V relative to the initial, rest, OCP). To determine the working electrode's rest OCP, electrodes were let to equilibrate in the RTIL sample for at least 5 min after the end of the bubbling procedure. The length of the equilibration period was such to generally obtain a sufficiently stable OCP (dV/dt below |0.0001|). All OCP experiments were performed inside an acrylate glove box (Molecular Imaging, model GB306) kept under nitrogen gas that was dried with a Drierite™ gas-drying unit.

**Cyclic voltammetry.** Cyclic voltammetry experiments were carried out inside a custom-built acrylate glovebox kept under positive argon flow (4.0 L×$min^{-1}$, >99.999%, Coregas, Australia) using an Emstat3 Blue potentiostat (PalmSens BV, Netherlands) and a single-compartment, three-electrode glass cell. The cell was loaded with ~25 mL of either ferrocene (Fc), cobaltocenium hexafluorophosphate ($Cc^+$), or decamethylcobaltocenium hexafluorophosphate ($Me_{10}Cc^+$) solutions ($1.0 \times 10^{-3}$

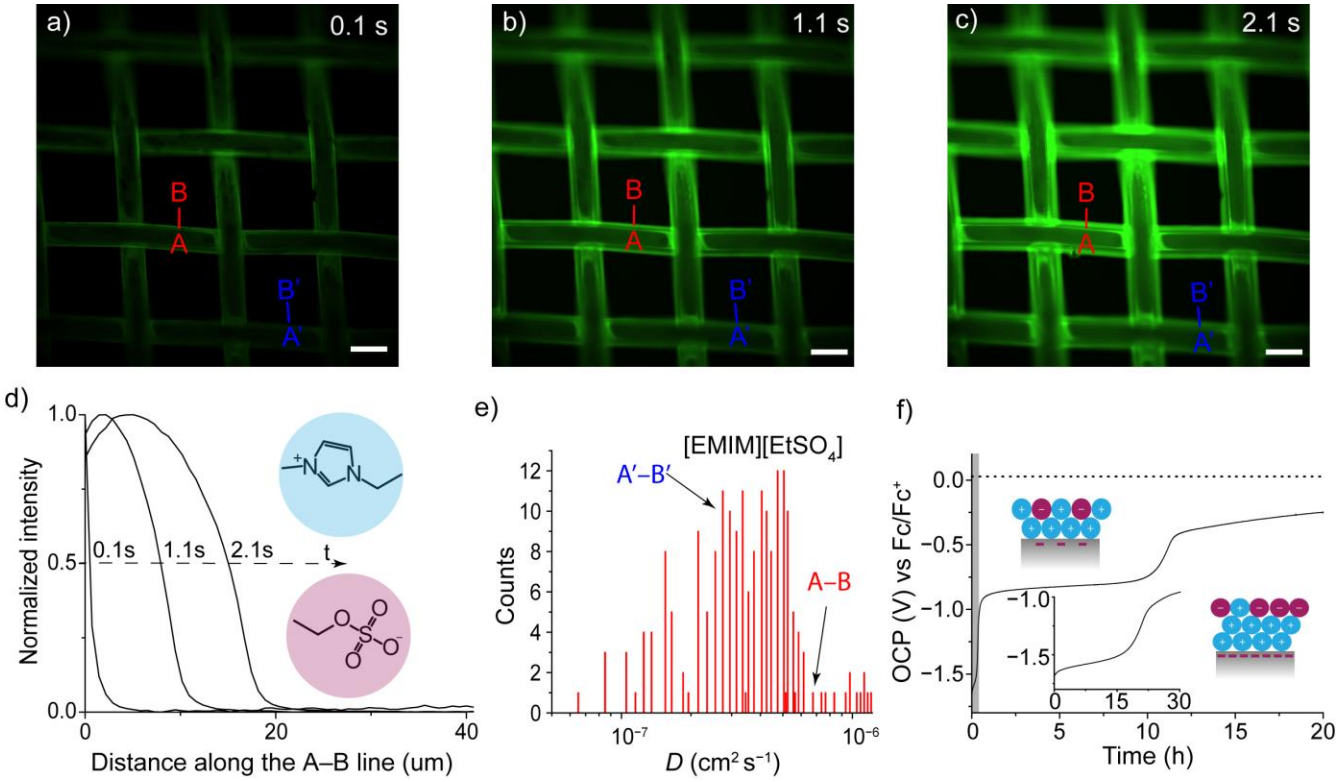


**Figure 2.** (a–c) Selected time-stamped fluorescence micrographs (10× magnification) recorded during the cathodic electrolysis (−2.0 V vs Ag/AgCl) of an oxygen-saturated **AMP–luc** solution (0.4 × 10−3 M in [EMIM][EtSO4]) at a platinum mesh electrode (Video S2, Supporting Information). Scale bars in (a–c) are 100 μm. (d) Representative fluorescence intensity plot profiles, sampled along the A–B line marked in (a–c), recorded 0.1, 1.1 and 2.1 s after the working electrode bias is stepped from open circuit to −2.0 V. The analysis of the movement over time of the superoxide diffusion front (triggering the **ox–luc** formation), as shown in (d) for a representative location, was repeated for at least 20 different working electrode locations per experiment, and at least 10 independent experiments were used to build the histogram plot shown in (e). The *D* values shown in (e) are calculated from the distance travelled by the fluorescence front between 0.1 s and 2.1 s, and as shown in (d), diffusivity is approximatively uniform over this time interval. (f) Representative OCP–time measurement for a platinum mesh working electrode immersed in [EMIM][EtSO4] (930 ppm of water). The electrode's OCP was recorded continuously for 20 h, starting after the application of a 60 s negative pulse (−2.0 V vs the initial OCP). The horizontal dotted line represents the initial (rest) OCP value. The cartoons show the schematic depictions of overscreening and crowding near-electrode cation-rich structures RTILs.[11, 13] The overscreening OCP signature remains stable for several hours, while the crowding plateau (inset) lasts for only ~15 min. The grey shaded area in (f) indicates the data expanded in the figure's inset (crowding).

M) in RTILs. Solutions were degassed prior to the measurements by means of a 20-min argon bubbling procedure. The working electrode was a platinum disk (eDAQ, ET052, 3 mm diameter), the counter electrode a platinum coil and the reference electrode a "leakless" Ag/AgCl electrode (eDAQ, part ET072-1). The working electrode was first polished with alumina slurry (0.05 μm, Dace Technology, Arizona) and then cleaned as described in the Fluorescence and ECL imaging section.

**Digital simulations of voltammograms.** Digital simulations of cyclic voltammograms were run on DigiElch8 (Gamry Instruments, Pennsylvania). Kinetic, thermodynamic and transport parameters were simulated by fitting data sets that covered a broad range of scan rates (from $1.0 \times 10^{-2}$ to 5.0 V $s^{-1}$), and assuming an E mechanism. Charge transfer kinetic parameters were estimated using Butler–Volmer kinetics. Diffusion was modelled as semi-infinite 1D diffusion, and the symmetry factor, α, was set to 0.5. The cell iR drop was left uncompensated during the measurements and the actual value measured by electrochemical impedance spectroscopy prior to each experiment and then used for the simulations. Cells resistance values were approximately 400 Ω for [EMIM][$EtSO_4$], 570 Ω for [BMPyrr][$NTf_2$] and 150 Ω for $Bu_4NPF_6$/MeCN.

## RESULTS AND DISCUSSION

As shown in the top-right section of Figure 1b, the cathodic electrolysis of an oxygenated solution of **AMP–luc** in an organic solvent-based electrolyte (DMSO/$Bu_4NClO_4$) leads to a red glow visible to the naked eye (Figures S2–S3, Supporting Information). The same electrolysis performed in RTILs, rather than in organic solvents, is however significantly less emissive (Figure 1b, and Figure S3, Supporting Information).[61] The ECL reaction is triggered by electrode-generated superoxide (Figure 1a and Figures S4, S5 and S6 Supporting Information).[39] As superoxide diffuses away from its generation site, the ECL's

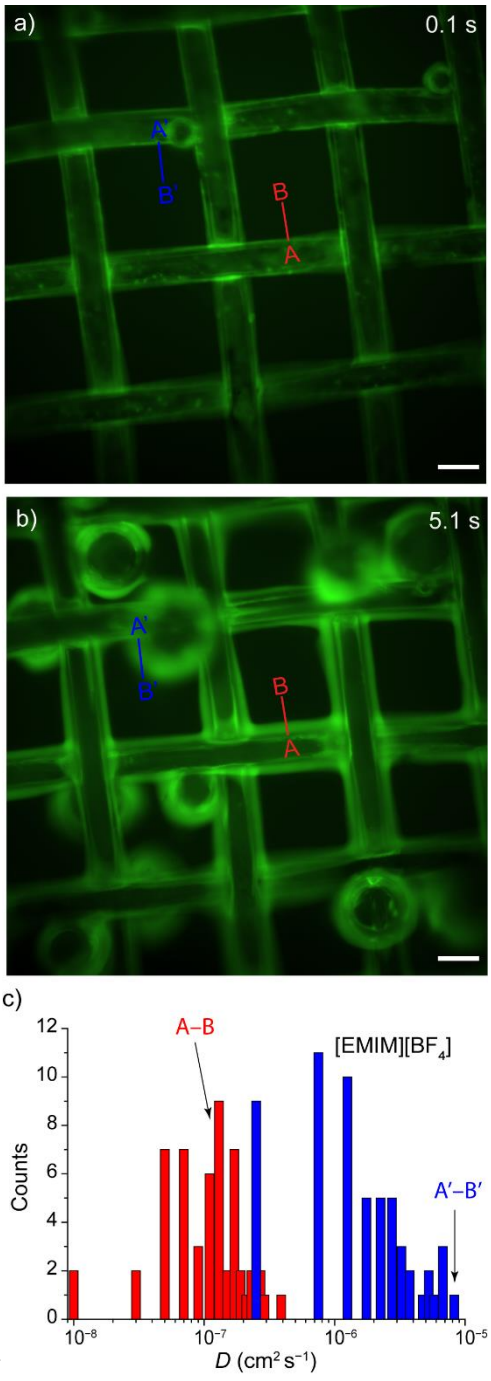


**Figure 3.** Time-stamped fluorescence micrographs (10× magnification) recorded (a) 0.1 s and (b) 5.1 s after the application of an external bias (−2.0 V vs Ag/AgCl) to an oxygen-saturated **AMP–luc** solution (0.4 × 10−3 M in [EMIM][BF4], 2400 ppm of water, Video S3, Supporting Information). Scale bars are 100 µm. The movement of the fluorescent front was tracked at ~60 electrode locations (8–9 locations across 7 videos of 7 samples) close to sites where gas bubble are visible (e.g. along the A'–B' line), and at ~60 locations (8–9 locations across 7 videos) at least 100 µm away from bubbles (e.g. A–B line). (c) Histogram plot for the optically determined superoxide D values in [EMIM][BF4]. Blue bars indicate measurements taken at electrode sites with clear convective (bubbles growing) disturbances, and red bars for measurements at quiescent sites. The *D* values in (c) are calculated from the distance travelled by the front after an electrolysis time of 5.1 s.

front also moves away from the platinum–RTIL interface. But while on one hand in DMSO/$Bu_4NClO_4$ it is possible to track the movement of this front (Figure S7 and Video S4, Supporting Information), and therefore to estimate optically a diffusion coefficient for superoxide ($2.62 \times 10^{-6}$ cm$^2$ s$^{-1}$ in agreement with previous reports),[39] on the other hand in RTILs the **AMP–luc** ECL reaction is too dim. Consequently, tracking optically the movement of the ECL front does not constitute a viable means of estimating diffusivities in RTILs. However, and very fortunately, the ECL product, **ox–luc** (Figure 1d), is fluorescent. Excitation with blue light of **AMP–luc** solutions undergoing electrolysis results in a bright green fluorescence which can be imaged with a CMOS camera and selecting exposure times as low as 20 ms (Figure 2a). Access to such fast capture rates, by focusing on redox pro-fluorescence rather than on ECL, means that the superoxide diffusion front can be visually mapped even in highly viscous RTILs (Figure 2a–c). Spatiotemporal *D* information become therefore available, data which are not accessible through conventional hydrodynamic measurements of diffusivity, such as rotating disk electrodes.[62] For example, from microscopy data as in Figure 2a–c the evolution of the fluorescence front can be rapidly sampled at several hundred different locations across the platinum electrode. The plot in Figure 2d shows the movement of the front at one of the ~200 locations analyzed (marked as A–B). The distance (*r*) travelled over time (*t*) by the front (taken arbitrarily as the point with an intensity half of the maximum value) along the A–B line away from the electrode, was used to compute diffusivity assuming an Einstein's random walk ($r^2 = 2Dt$). Data at electrolysis times beyond ~3 s were discarded since, as shown by Amatore and coworkers, natural convection becomes then dominant leading to underestimate the diffuse layer thickness.[63-65] The histogram in Figure 2e shows the distribution across the macroscopic sample of the optically determined *D*. The mode of *D* is $4.80 \times 10^{-7}$ cm$^2$ s$^{-1}$, but while for example the fluorescent front moves along the A–B line with a *D* of $5.25 \times 10^{-7}$ cm$^2$ s$^{-1}$, the same measurement along A'–B' indicates a slightly smaller *D* ($3.35 \times 10^{-7}$ cm$^2$ s$^{-1}$). Such local differences in *D*, most likely due to natural convection,[63-65] would however be lost in a conventional electrochemical measurement and even advanced forms of redox microscopy would not be able to access these information.[46-48] A small level of lateral asymmetry in the overall fluorescence intensity is visible in micrographs (e.g. Video S2) but was not due to the relative position of counter and working electrodes (Figure S8, Supporting Information), as observed before for ECL systems.[50] In addition to natural convection, it is possible that a lateral heterogeneity in current density (across the Pt mesh) may lead to material transport via diffusioosmotic fluid flow,[66, 67] which in turn may lead to the observed asymmetry. The average *D* obtained in [EMIM][$EtSO_4$] is one order of magnitude smaller than in DMSO,[39] as it expected based on the higher viscosity of the former (~100 cP vs. 2.0 cP).[68]

During the cathodic electrolysis of **AMP–luc** [EMIM][$EtSO_4$] the interface remains relatively quiescent and the distribution of *D* across the electrode surface is therefore relatively narrow (Figure 2e). This is surprising, as despite both the large negative potential used to trigger the pro-fluorescent reaction (−2.0 V vs Ag/AgCl for 15 s) and the moderate level of water content in [EMIM][$EtSO_4$] (930 ppm), yet there was no evidence of hydrogen bubbles forming on the electrode (Video S2). The formation and departure from the electrode of

gas bubbles would have introduced convection hence caused highly dispersed D values.

This leads to the question of what prevents in [EMIM][$EtSO_4$] gas evolution at such negative voltage biases. As introduced above, some RTILs form compact and long-lived cation-rich double layer structures on negatively biased electrodes. The compactness of such RTILs structures has been detected by Atkin and co-workers as a mechanical resistance to AFM tips approaching biased electrodes,[16, 69]and manifest stable and discrete open circuit potential (OCP) plateaus.[13] For example, OCP–time data in Figure 2f show that with [EMIM][$EtSO_4$], the imidazolium-rich layer formed at a platinum cathode persists for nearly 10 h once the cathodic bias has been removed. Only mechanical shaking of the electrochemical cell disrupts prematurely such ordered double-layer arrangement.[13] More specifically, once the exogenous field (the negative electrode bias) is removed and the OCP logging started, both crowding and overscreening structures persist for ~15 min and ~10 h, respectively (Figure 2f).[11, 13] Notably, in the fluorescence experiments described above the cathodic bias is not interrupted, hence cation-rich interfacial layers are likely to be present for the entire duration of the **AMP–luc** electrolysis. Although unlikely to interfere with the relatively anodic reduction of oxygen (Figure S9, Supporting Information), we believe this compact layer, especially crowding, is introducing a kinetic barrier to inner-sphere redox reactions, preventing, despite the presence of substantial levels of water, gas evolution even under very negative voltages. The formation of crowding and overscreening structures in [EMIM][$EtSO_4$] hinders the reduction of water traces to the point that this relatively hydrophilic RTIL (~1000 ppm of water) behaves alike an hydrophobic RTIL such as [BMPyrr][$NTf_2$] (~100 ppm of water, Figure S10 and Video S5, Supporting Information). For both RTILs, the lack of bubble-induced convective disturbances accounts for a relatively narrow distribution of *D* values across the macroscopic electrode.

By mapping the **ox–luc** fluorescent front, a large dispersion in the diffusivity characteristics were however revealed for RTILs that do not form compact double-layers. For instance, in [EMIM][$BF_4$] (34 cP, ~2400 ppm of water) mapping diffusion fronts at random locations across the electrode unveiled superoxide *D* values spread over nearly four orders of magnitude (Figure 3). [EMIM][$BF_4$] does not have a significant barrier to water reduction (Figure S11, Supporting Information) and hydrogen bubbles form on the electrode during the cathodic electrolysis of **AMP–luc**. Notably, when *D* is measured far away from a growing bubble, such as at the A–B line marked in Figure 3a–b, its value is, as expected, lower than for the less viscous [EMIM][$EtSO_4$] and experimental *D* values felt within a relatively narrow range (Figure 3c, red bars). Growing bubbles are clearly visible in the fluorescence micrographs (Figure 3b), and tracking the movement of **ox–luc** near the gas cavities – sites where quiescent diffusion is disturbed by convection – led to a significant local overestimate of *D* (Figure 3c, blue bars).

This spread in the superoxide diffusion coefficient in [EMIM][$BF_4$] is caused by the lack of a barrier towards inner-sphere reactions and not by the large hydrophilicity of this RTIL. For instance [EMIM][$EtSO_4$] does not show any evolution of bubbles even when deliberately spiked with 2% of water (Figure S12a and Video S6, Supporting Information). Even with such large level of water, the [EMIM][$EtSO_4$]–electrode interface retains its ability to form compact electrostatic structures detectable as long-lived negative OCP plateaus (Figure S12b). [EMIM][$BF_4$] on the other hand cannot favourably align with the electrode electric field even at water levels as low as 500 ppm.[13] The growth rate of the bubbles is not uniform, hence unlike for quiescent systems (Figure 2d), apparent *D* values measured on bubbles are not uniform over time (Figure S13, Supporting Information).The formation of stable double layers is strongly influenced by the nature of the RTIL, and for example cations with smaller alkyl chains can more easily pack at a negative charged surface compared to larger cations.[70] However, [EMIM][$EtSO_4$] and [EMIM][$BF_4$] share the same cation, thus the strikingly different ability to form stable double layers is due to difference in the anion. Specifically, the reason lies in the [$BF_4$] anion lacking a dipole moment. The stronger dipole moment of [$EtSO_4$] facilitates its alignment with the external electric field, and consequently the generation of an internal electric filed, which manifests as a long-lived OCP signature.[13]

It is only when the water level becomes as high as 5.0% that the duration of overscrening plateaus in [EMIM][$EtSO_4$] is significantly reduced, while the evolution of gas bubbles becomes significant (Figure S12c,d and Video S7, Supporting Information). With [BMPyrr][$NTf_2$], another RTIL where cathodic biasing does not lead to discrete negative OCP signatures (Figure S10f), a water content of 2.0% is already sufficient to cause significant gas evolution under the negative bias of the pro-fluorescent experiments (Figure S12e,f and Video S8, Supporting Information). While, as shown above, an inner-sphere reaction such as hydrogen evolution is influenced by how accessible the electrode surface is, the presence or absence of ordered and compact RTIL structures is unlikely to have a significant effect on outer-sphere reactions.[18] To test this we turned to well-studied outer-sphere metallocenes.[71] Crowding and overscreening are unlikely to impair the redox kinetics of molecules such as ferrocenes and cobaltocenes. The choice of $Cc^+$ and $Me_{10}Cc^+$ is because they both have, especially $Me_{10}Cc^+$,[72, 73] redox potentials sufficiently negative so to approach the cathodic bias used for the **AMP–luc** pro-fluorescent reaction and to closely match the position of the overscreening and crowding OCP signatures. By digital simulations of cyclic voltammetry experiments at different scan rates (from $1.0 \times 10^{-2}$ to 5.0 V $s^{-1}$) we looked for evidence of a drop in the electron transfer rate constants ($k_{et}$) when the solvent was changed from MeCN to RTILs of similar viscosity (~100 cP) but that either form or do not form cation-rich structures that leads to discrete OCP signatures after a cathodic pulse ([EMIM][$EtSO_4$] and [BMPyrr][$NTf_2$] respectively).[74] The fitting results are summarized in Figure 4. Firstly, in an organic solvent (MeCN/$Bu_4NPF_6$) the refined $k_{et}$ is about one order of magnitude higher than in both RTILs. Secondly, a comparison between $k_{et}$ obtained in [EMIM][$EtSO_4$] and in [BMPyrr][$NTf_2$] suggests for both Fc and Cc comparable, with the uncertainty, redox kinetics in both RTILs. Unfortunately data for $Me_{10}Cc$ in [BMPyrr][$NTf_2$] were not reproducible, possibly due to the poor stabilization of $Me_{10}Cc^+$ by the [$NTf_2$] anion.[75] The drop in $k_{et}$ moving from MeCN to [EMIM][$EtSO_4$] was comparable for Fc, $Cc^+$ and $Me_{10}Cc^+$. This is important, since in the case of a blocking effect by cathodic overscreening and crowding structures on the electron transfer of outer-sphere couples, a drop in $k_{et}$ would have been negligible for the relatively anodic $Fc/Fc^+$ couple, but progressively larger for $Cc^+$

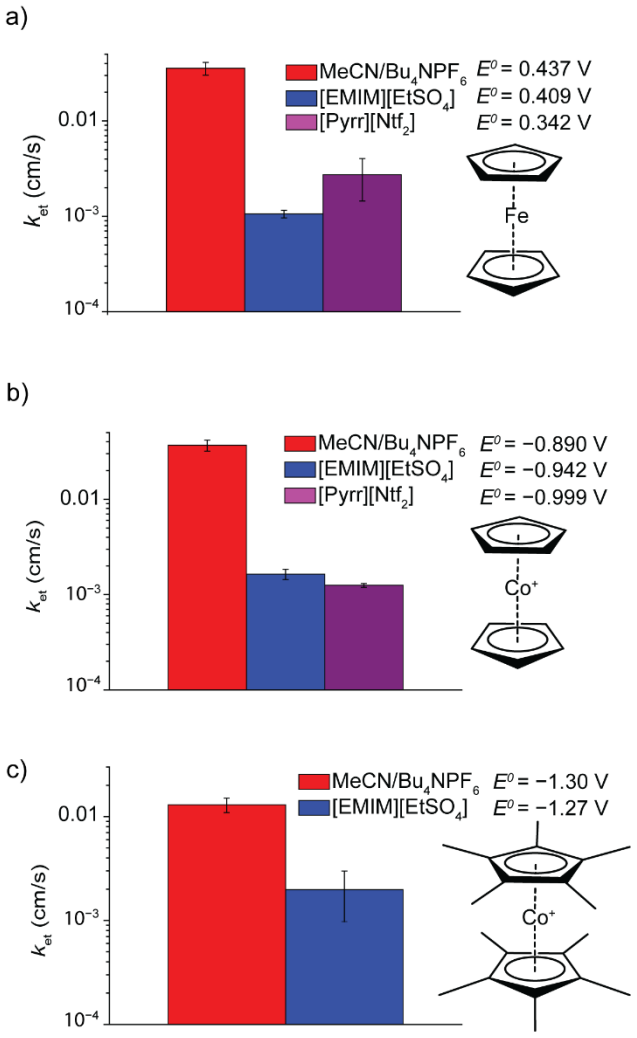


**Figure 4.** Comparison of the refined (digital simulations of experimental cyclic voltammograms, CVs) charge transfer rate constant ($k_{et}$) of three outer-sphere redox molecules (Fc (a), $Cc^+$ (b), and $Me_{10}Cc^+$ (c)). Voltammograms were obtained in $1.0 \times 10^{-1}$ M MeCN/$Bu_4NPF_6$ (red bars), [EMIM][$EtSO_4$] (blue bars), and [BMPyrr][$NTf_2$] (violet bars). Experiments were repeated at least five times for each system, and the CV voltage sweep rate was varied between 0.01 and 5.0 $Vs^{-1}$. (Supporting Information, Figure S14–S21). The metallocene concentration was $1.0 \times 10^{-3}$ M. No $k_{et}$ value is reported for $Me_{10}Cc^+$ in [BMPyrr][$NTf_2$] as CVs of this system were poorly reproducible. Refined values of the apparent formal potential ($E^{0'}$ vs Ag/AgCl) are indicated by labels in figure. The chemical structure of each metallocene is shown next to the relative graph.

and $Me_{10}Cc^+$. The redox couple $Cc/Cc^+$, has a redox potential 1.33-1.35 V more negative than that of the $Fc/Fc^+$ couple (Figure 4a,b), and the $Me_{10}Cc/Me_{10}Cc^+$ couple is about 1.67 V more negative than the $Fc/Fc^+$ couple, and therefore close to the potential where ordered double layers form in [EMIM][$EtSO_4$] (Figure 2f) and yet the relative drop in $k_{et}$ is comparable or even smaller for the latter.

## CONCLUSIONS

We have developed a spatiotemporally resolved optical measurement of diffusion coefficients that can account for convective disturbances. This approach reduces the likelihood of overestimating diffusion coefficients in viscous systems where adventitious gas-evolving reactions cannot be ruled out. The cathodic generation of fluorescent oxyluciferin (**ox–luc**), by means of reacting firefly's luciferin adenylate ester (**AMP–luc**) with electrode-generated superoxide radical anion, was used to map superoxide diffusivity in RTILs. Literature diffusivity data for superoxide in RTILs are highly scattered, presumably because the presence of water impurities[1, 76, 77] leads to unaccounted and poorly reproducible convective contribution to mass transport. Visual mapping of electro-generated **ox–luc** diffusion fronts addresses this this issue and allows to measure accurately diffusion coefficients even in systems where convection cannot be removed. For example we demonstrate that in [EMIM][$BF_4$], $D$ for superoxide increases from $6.40 \times 10^{-8}$ $cm^2$ $s^{-1}$ in quiescent regions, to $2.30 \times 10^{-6}$ $cm^2$ $s^{-1}$ in regions affected by convective disturbances (in proximity of evolving gas bubbles). A conventional macroscopic one-electrode, one-lead measurement would output an average and therefore overestimate diffusion coefficient. While evolution of gaseous products, and its interference with quiescent diffusion, cannot be removed, it can however be detected, accounted for, and even predicted. With regards to this last point – the likelihood of significant convective disturbances – we have been able to uncover a link between inner-sphere reduction of water and the stability of cation-rich double layer RTIL structures. Our results suggest that RTILs forming stable overscreening and crowding double layers can be biased to very negative voltages without detectable gas evolution from water splitting or proton reduction. Readily available time-resolved open-circuit potentiometry can be used to screen for RTILs likely to yield stable overscreening and crowding layers under negative electrode biases. We also note that while compact double layer RTIL structures pose a significant kinetic barrier to inner sphere reactions, such structures do not impair the electrode kinetics of outer-sphere redox reactions, such as for widespread metallocenes.

## ASSOCIATED CONTENT

### Supporting Information

The Supporting Information is available free of charge on the ACS Publications website. Detailed description of electrochemical set up, experimental and simulated cyclic voltammograms, open circuit potentiometry data, fluorescence and ECL images, time resolved fluorescence and ECL intensity profiles, photon counting plots (PDF). Supplementary videos (.mp4).

## AUTHOR INFORMATION

### Corresponding Author

**Simone Ciampi** −School of Molecular and Life Sciences, Curtin University, Bentley, Western Australia 6102, Australia; Email: simone.ciampi@curtin.edu.au

### Author

**Mattia Belotti** − School of Molecular and Life Sciences, Curtin University, Bentley, Western Australia 6102, Australia

**Mohsen M. T. El-Tahawy** − Dipartimento di Chimica Industriale "Toso Montanari", Università di Bologna, Bologna, Emilia Romagna, 40136, Italy − Chemistry Department, Faculty of Science, Damanhour University, Damanhour 22511, Egypt

**Marco Garavelli** − Dipartimento di Chimica Industriale "Toso Montanari", Università di Bologna, Bologna, Emilia Romagna, 40136, Italy

**Michelle L. Coote** − Institute for Nanoscale Science and Technology, College of Science and Engineering, Flinders University Bedford Park, South Australia, 5042, Australia

**K. Swaminathan Iyer** − School of Molecular Sciences, The University of Western Australia, Perth, Western Australia 6009, Australia

### Author Contributions

The manuscript was written through contributions of all authors. All authors have given approval to the final version of the manuscript.

## ACKNOWLEDGMENT

This work was financially supported by the Australian Research Council (grants no. DP220100553 and FT190100148).

## REFERENCES

1. Buzzeo, M. C.; Evans, R. G.; Compton, R. G., Non-Haloaluminate Room-Temperature Ionic Liquids in Electrochemistry—A Review. *ChemPhysChem* **2004,** *5*, 1106–1120.
2. Yang, G.; Song, Y.; Wang, Q.; Zhang, L.; Deng, L., Review of ionic liquids containing, polymer/inorganic hybrid electrolytes for lithium metal batteries. *Mater. Des.* **2020,** *190*, 108563.
3. Zhong, C.; Deng, Y.; Hu, W.; Qiao, J.; Zhang, L.; Zhang, J., A Review of Electrolyte Materials and Compositions for Electrochemical Supercapacitors. *Chem. Soc. Rev.* **2015,** *44*, 7484–7539.
4. Zhou, F.; Izgorodin, A.; Hocking, R. K.; Spiccia, L.; MacFarlane, D. R., Electrodeposited MnOx Films from Ionic Liquid for Electrocatalytic Water Oxidation. *Adv. Energy Mater.* **2012,** *2*, 1013–1021.
5. Rama, R.; Meenakshi, S.; Pandian, K.; Gopinath, S. C. B., Room Temperature Ionic Liquids-Based Electrochemical Sensors: An Overview on Paracetamol Detection. *Crit. Rev. Anal. Chem.* **2022,** *52*, 1422–1431.
6. Buzzeo, M. C.; Hardacre, C.; Compton, R. G., Use of Room Temperature Ionic Liquids in Gas Sensor Design. *Anal. Chem.* **2004,** *76*, 4583–4588.
7. Sangoro, J. R.; Serghei, A.; Naumov, S.; Galvosas, P.; Kärger, J.; Wespe, C.; Bordusa, F.; Kremer, F., Charge transport and mass transport in imidazolium-based ionic liquids. *Phys. Rev. E* **2008,** *77*, 051202.
8. Monaco, S.; Soavi, F.; Mastragostino, M., Role of Oxygen Mass Transport in Rechargeable Li/O2 Batteries Operating with Ionic Liquids. *J. Phys. Chem. Lett.* **2013,** *4*, 1379–1382.
9. Park, J.-W.; Yoshida, K.; Tachikawa, N.; Dokko, K.; Watanabe, M., Limiting current density in bis(trifluoromethylsulfonyl)amide-based ionic liquid for lithium batteries. *J. Power Sources* **2011,** *196*, 2264–2268.
10. Fedorov, M. V.; Kornyshev, A. A., Ionic Liquids at Electrified Interfaces. *Chem. Rev.* **2014,** *114*, 2978–3036.
11. Bazant, M. Z.; Storey, B. D.; Kornyshev, A. A., Double Layer in Ionic Liquids: Overscreening versus Crowding. *Phys. Rev. Lett.* **2011,** *106*, 046102.
12. Fedorov, M. V.; Kornyshev, A. A., Ionic Liquid Near a Charged Wall: Structure and Capacitance of Electrical Double Layer. *J. Phys. Chem. B* **2008,** *112*, 11868–11872.
13. Belotti, M.; Lyu, X.; Xu, L.; Halat, P.; Darwish, N.; Silvester, D. S.; Goh, C.; Izgorodina, E. I.; Coote, M. L.; Ciampi, S., Experimental Evidence of Long-Lived Electric Fields of Ionic Liquid Bilayers. *J. Am. Chem. Soc.* **2021,** *143*, 17431–17440.
14. Atkin, R.; Warr, G. G., Structure in Confined Room-Temperature Ionic Liquids. *J. Phys. Chem. C* **2007,** *111*, 5162–5168.
15. Zhang, X.; Zhong, Y.-X.; Yan, J.-W.; Su, Y.-Z.; Zhang, M.; Mao, B.-W., Probing Double Layer Structures of Au (111)–BMIPF6 Ionic Liquid Interfaces from Potential-Dependent AFM Force Curves. *Chem. Comm.* **2012,** *48*, 582–584.
16. Li, H.; Wang, J.; Warr, G. G.; Atkin, R., Extremely slow dynamics of ionic liquid self-assembled nanostructures near a solid surface. *J. Colloid Interface Sci.* **2023,** *630*, 658–665.
17. Toda, S.; Clark, R.; Welton, T.; Shigeto, S., Observation of the Pockels Effect in Ionic Liquids and Insights into the Length Scale of Potential-Induced Ordering. *Langmuir* **2021,** *37*, 5193–5201.
18. Bard, A. J., Inner-Sphere Heterogeneous Electrode Reactions. Electrocatalysis and Photocatalysis: The Challenge. *J. Am. Chem. Soc.* **2010,** *132*, 7559–7567.
19. Ahmad, H.; Kamarudin, S. K.; Minggu, L. J.; Kassim, M., Hydrogen from photo-catalytic water splitting process: A review. *Renewable Sustainable Energy Rev.* **2015,** *43*, 599–610.
20. Bard, A. J.; Faulkner, L. R.; White, H. S., *Electrochemical methods: fundamentals and applications*. John Wiley & Sons: 2022.
21. Xiao, X.; Pan, S.; Jang, J. S.; Fan, F.-R. F.; Bard, A. J., Single Nanoparticle Electrocatalysis: Effect of Monolayers on Particle and Electrode on Electron Transfer. *J. Phys. Chem. C* **2009,** *113*, 14978–14982.
22. Ren, Y.; Yu, C.; Tan, X.; Huang, H.; Wei, Q.; Qiu, J., Strategies to suppress hydrogen evolution for highly selective electrocatalytic nitrogen reduction: challenges and perspectives. *Energy Environ. Sci.* **2021,** *14*, 1176–1193.
23. Angulo, A.; van der Linde, P.; Gardeniers, H.; Modestino, M.; Fernández Rivas, D., Influence of Bubbles on the Energy Conversion Efficiency of Electrochemical Reactors. *Joule* **2020,** *4*, 555–579.
24. Kiros, Y.; Bursell, M., Low energy consumption in chlor-alkali cells using oxygen reduction electrodes. *Int. J. Electrochem. Sci* **2008,** *3*, 444–451.
25. Thorne, R. J.; Sommerseth, C.; Ratvik, A. P.; Rørvik, S.; Sandnes, E.; Lossius, L. P.; Linga, H.; Svensson, A. M., Bubble Evolution and Anode Surface Properties in Aluminium Electrolysis. *J. Electrochem. Soc.* **2015,** *162*, E104.
26. Vogt, H., The Quantities Affecting the Bubble Coverage of Gas-Evolving Electrodes. *Electrochim. Acta* **2017,** *235*, 495–499.
27. Sato, T.; Masuda, G.; Takagi, K., Electrochemical properties of novel ionic liquids for electric double layer capacitor applications. *Electrochim. Acta* **2004,** *49*, 3603–3611.
28. Zhao, X.; Ren, H.; Luo, L., Gas bubbles in electrochemical gas evolution reactions. *Langmuir* **2019,** *35*, 5392–5408.
29. de Souza, R. F.; Padilha, J. C.; Gonçalves, R. S.; de Souza, M. O.; Rault-Berthelot, J., Electrochemical hydrogen production from water electrolysis using ionic liquid as electrolytes: Towards the best device. *J. Power Sources* **2007,** *164*, 792–798.
30. de Souza, R. F.; Loget, G.; Padilha, J. C.; Martini, E. M. A.; de Souza, M. O., Molybdenum electrodes for hydrogen production by water electrolysis using ionic liquid electrolytes. *Electrochem. Commun.* **2008,** *10*, 1673–1675.
31. Filla, M.; Davidson, J. F.; Bates, J. F.; Eccles, M. A., Gas phase controlled mass transfer from a bubble. *Chem. Eng. Sci.* **1976,** *31*, 359–367.
32. Burdyny, T.; Graham, P. J.; Pang, Y.; Dinh, C.-T.; Liu, M.; Sargent, E. H.; Sinton, D., Nanomorphology-Enhanced Gas-Evolution Intensifies $CO_2$ Reduction Electrochemistry. *ACS Sustainable Chem. Eng.* **2017,** *5*, 4031–4040.

33. Vogel, Y. B.; Evans, C. W.; Belotti, M.; Xu, L.; Russell, I. C.; Yu, L.-J.; Fung, A. K. K.; Hill, N. S.; Darwish, N.; Gonçales, V. R.; Coote, M. L.; Swaminathan Iyer, K.; Ciampi, S., The corona of a surface bubble promotes electrochemical reactions. *Nat. Commun.* **2020,** *11*, 6323.
34. Vogel, Y. B.; Molina, A.; Gonzalez, J.; Ciampi, S., Microelectrode arrays with active-area geometries defined by spatial light modulation. *Electrochim. Acta* **2020,** *356*, 136849.
35. Choudhury, M. H.; Ciampi, S.; Yang, Y.; Tavallaie, R.; Zhu, Y.; Zarei, L.; Gonçales, V. R.; Gooding, J. J., Connecting electrodes with light: one wire, many electrodes. *Chem. Sci.* **2015,** *6*, 6769–6776.
36. Amatore, C.; Savéant, J. M.; Tessier, D., Charge transfer at partially blocked surfaces: A model for the case of microscopic active and inactive sites. *J. Electroanal. Chem. Interfacial Electrochem.* **1983,** *147*, 39–51.
37. Hendriks, F. C.; Meirer, F.; Kubarev, A. V.; Ristanović, Z.; Roeffaers, M. B. J.; Vogt, E. T. C.; Bruijnincx, P. C. A.; Weckhuysen, B. M., Single-Molecule Fluorescence Microscopy Reveals Local Diffusion Coefficients in the Pore Network of an Individual Catalyst Particle. *J. Am. Chem. Soc.* **2017,** *139*, 13632–13635.
38. Elliott, J. R.; Compton, R. G., Local diffusion indicators: A new tool for analysis of electrochemical mass transport. *J. Electroanal. Chem.* **2022,** *908*, 116114.
39. Belotti, M., El-Tahawy, M..M.T., Yu, L.-J., Russell, I..C., Darwish, N., Coote, M..L., Garavelli, M. and Ciampi, S., Luciferase-free Luciferin Electrochemiluminescence. *Angew. Chem. Int. Ed.* **2022,** *61*, e202209670.
40. Engstrom, R. C.; Ghaffari, S.; Qu, H., Fluorescence imaging of electrode-solution interfacial processes. *Anal. Chem.* **1992,** *64*, 2525–2529.
41. Bowyer, W. J.; Xie, J.; Engstrom, R. C., Fluorescence imaging of the heterogeneous reduction of oxygen. *Anal. Chem.* **1996,** *68*, 2005–2009.
42. Vitt, J. E.; Engstrom, R. C., Imaging of Oxygen Evolution and Oxide Formation Using Quinine Fluorescence. *Anal. Chem.* **1997,** *69*, 1070–1076.
43. Engstrom, R. C.; Johnson, K. W.; DesJarlais, S., Characterization of electrode heterogeneity with electrogenerated chemiluminescence. *Anal. Chem.* **1987,** *59*, 670–673.
44. Engstrom, R. C.; Pharr, C. M.; Koppang, M. D., Visualization of the edge effect with electrogenerated chemiluminescence. *J. Electroanal. Chem. Interfacial Electrochem.* **1987,** *221*, 251–255.
45. Pharr, C. M.; Engstrom, R. C.; Tople, R. A.; Bee, T. K.; Unzelman, P. L., Time-resolved imaging of current density at inlaid disk electrodes. *J. Electroanal. Chem. Interfacial Electrochem.* **1990,** *278*, 119–128.
46. Vogel, Y. B.; Gooding, J. J.; Ciampi, S., Light-addressable electrochemistry at semiconductor electrodes: redox imaging, mask-free lithography and spatially resolved chemical and biological sensing. *Chem. Soc. Rev.* **2019,** *48*, 3723–3739.
47. Vogel, Y. B.; Gonçales, V. R.; Gooding, J. J.; Ciampi, S., Electrochemical Microscopy Based on Spatial Light Modulators: A Projection System to Spatially Address Electrochemical Reactions at Semiconductors. *J. Electrochem. Soc.* **2018,** *165*, H3085.
48. Vogel, Y. B.; Darwish, N.; Ciampi, S., Spatiotemporal Control of Electrochemiluminescence Guided by a Visible Light Stimulus. *Cell Rep. Phys. Sci.* **2020,** *1*, 100107.
49. Amatore, C.; Chovin, A.; Garrigue, P.; Servant, L.; Sojic, N.; Szunerits, S.; Thouin, L., Remote Fluorescence Imaging of Dynamic Concentration Profiles with Micrometer Resolution Using a Coherent Optical Fiber Bundle. *Anal. Chem.* **2004,** *76*, 7202–7210.
50. Doneux, T.; Bouffier, L.; Goudeau, B.; Arbault, S., Coupling Electrochemistry with Fluorescence Confocal Microscopy To Investigate Electrochemical Reactivity: A Case Study with the Resazurin-Resorufin Fluorogenic Couple. *Anal. Chem.* **2016,** *88*, 6292–6300.
51. Rudd, N. C.; Cannan, S.; Bitziou, E.; Ciani, I.; Whitworth, A. L.; Unwin, P. R., Fluorescence Confocal Laser Scanning Microscopy as a Probe of pH Gradients in Electrode Reactions and Surface Activity. *Anal. Chem.* **2005,** *77*, 6205–6217.
52. Cannan, S.; Douglas Macklam, I.; Unwin, P. R., Three-dimensional imaging of proton gradients at microelectrode surfaces using confocal laser scanning microscopy. *Electrochem. Commun.* **2002,** *4*, 886–892.
53. Kragt, H. J.; Smith, C. P.; White, H. S., Refractive index mapping of concentration profiles. *J. Electroanal. Chem. Interfacial Electrochem.* **1990,** *278*, 403–407.
54. Bath, B. D.; Lee, R. D.; White, H. S.; Scott, E. R., Imaging Molecular Transport in Porous Membranes. Observation and Analysis of Electroosmotic Flow in Individual Pores Using the Scanning Electrochemical Microscope. *Anal. Chem.* **1998,** *70*, 1047–1058.
55. Takahashi, Y.; Shevchuk, A. I.; Novak, P.; Babakinejad, B.; Macpherson, J.; Unwin, P. R.; Shiku, H.; Gorelik, J.; Klenerman, D.; Korchev, Y. E.; Matsue, T., Topographical and electrochemical nanoscale imaging of living cells using voltage-switching mode scanning electrochemical microscopy. *Proc. Natl. Acad. Sci.* **2012,** *109*, 11540–11545.
56. Al-Handawi, M. B.; Polavaram, S.; Kurlevskaya, A.; Commins, P.; Schramm, S.; Carrasco-López, C.; Lui, N. M.; Solntsev, K. M.; Laptenok, S. P.; Navizet, I.; Naumov, P., Spectrochemistry of Firefly Bioluminescence. *Chem. Rev.* **2022,** *122*, 13207–13234.
57. White, E. H.; Rapaport, E.; Seliger, H. H.; Hopkins, T. A., The chemi- and bioluminescence of firefly luciferin: An efficient chemical production of electronically excited states. *Bioorg. Chem.* **1971,** *1*, 92–122.
58. Schindelin, J.; Arganda-Carreras, I.; Frise, E.; Kaynig, V.; Longair, M.; Pietzsch, T.; Preibisch, S.; Rueden, C.; Saalfeld, S.; Schmid, B.; Tinevez, J.-Y.; White, D. J.; Hartenstein, V.; Eliceiri, K.; Tomancak, P.; Cardona, A., Fiji: an open-source platform for biological-image analysis. *Nat. Methods* **2012,** *9*, 676–682.
59. Berg, H. C., Random walks in biology. In *Random Walks in Biology*, Princeton University Press: 2018.
60. Compton, R. G.; Banks, C. E., *Understanding voltammetry*. World Scientific: 2018.
61. Belotti, M.; El-Tahawy, M. M. T.; Darwish, N.; Garavelli, M.; Ciampi, S., Electrochemically Generated Luminescence of Luminol and Luciferin in Ionic Liquids. *ChemElectroChem* **2022**, e202201033.
62. Sheng, W.; Gasteiger, H. A.; Shao-Horn, Y., Hydrogen Oxidation and Evolution Reaction Kinetics on Platinum: Acid vs Alkaline Electrolytes. *J. Electrochem. Soc.* **2010,** *157*, B1529.
63. Amatore, C.; Pebay, C. c.; Thouin, L.; Wang, A.; Warkocz, J., Difference between ultramicroelectrodes and microelectrodes: influence of natural convection. *Anal. Chem.* **2010,** *82*, 6933–6939.
64. Amatore, C.; Szunerits, S.; Thouin, L.; Warkocz, J.-S., The real meaning of Nernst's steady diffusion layer concept under non-forced hydrodynamic conditions. A simple model based on Levich's seminal view of convection. *J. Electroanal. Chem.* **2001,** *500*, 62–70.
65. Baltes, N.; Thouin, L.; Amatore, C.; Heinze, J., Imaging Concentration Profiles of Redox-Active Species with Nanometric Amperometric Probes: Effect of Natural Convection on Transport at Microdisk Electrodes. *Angew. Chem., Int. Ed.* **2004,** *43*, 1431–1435.
66. Moazzenzade, T.; Yang, X.; Walterbos, L.; Huskens, J.; Renault, C.; Lemay, S. G., Self-Induced Convection at Microelectrodes via Electroosmosis and Its Influence on Impact Electrochemistry. *J. Am. Chem. Soc.* **2020,** *142*, 17908−17912.
67. Williams, I.; Lee, S.; Apriceno, A.; Sear, R. P.; Battaglia, G., Diffusioosmotic and convective flows induced by a nonelectrolyte concentration gradient. *Proc. Natl. Acad. Sci.* **2020,** *117*, 25263–25271.
68. Prem Kumar, T.; Prabhu, P. V. S. S.; Srivastava, A. K.; Bejoy Kumar, U.; Ranganathan, R.; Gangadharan, R., Conductivity and viscosity studies of dimethyl sulfoxide (DMSO)-based electrolyte solutions at 25 °C. *J. Power Sources* **1994,** *50*, 283−294.

69. Hayes, R.; Warr, G. G.; Atkin, R., Structure and Nanostructure in Ionic Liquids. *Chem. Rev.* **2015,** *115*, 6357–6426.
70. Li, H.; Endres, F.; Atkin, R., Effect of alkyl chain length and anion species on the interfacial nanostructure of ionic liquids at the Au(111)–ionic liquid interface as a function of potential. *Phys. Chem. Chem. Phys.* **2013,** *15*, 14624–14633.
71. Hui, J.; Zhou, X.; Bhargava, R.; Chinderle, A.; Zhang, J.; Rodríguez-López, J., Kinetic Modulation of Outer-Sphere Electron Transfer Reactions on Graphene Electrode with a Sub-surface Metal Substrate. *Electrochim. Acta* **2016,** *211*, 1016–1023.
72. Cooper, J. B.; Bond, A. M., Evidence for adsorption of the cobaltocenium cation and precipitation of uncharged cobaltocene at the platinum microelectrode-acetonitrile interface in the absence of supporting electrolyte. *Anal. Chem.* **1993,** *65*, 2724–2730.
73. Hwang, B.; Park, M. S.; Kim, K., Ferrocene and Cobaltocene Derivatives for Non-Aqueous Redox Flow Batteries. *Chem. Sus. Chem.* **2015,** *8*, 310–314.
74. Zhang, X.; Leddy, J.; Bard, A. J., Dependence of rate constants of heterogeneous electron transfer reactions on viscosity. *J. Am. Chem. Soc.* **1985,** *107*, 3719–3721.
75. Sun, Q.-W.; Murase, K.; Ichii, T.; Sugimura, H., Anionic effect of ionic liquids electrolyte on electrochemical behavior of ferrocenylthiol/alkanethiol binary SAMs. *J. Electroanal. Chem.* **2010,** *643*, 58–66.
76. Zigah, D.; Wang, A.; Lagrost, C.; Hapiot, P., Diffusion of Molecules in Ionic Liquids/Organic Solvent Mixtures. Example of the Reversible Reduction of O2 to Superoxide. *J. Phys. Chem. B* **2009,** *113*, 2019–2023.
77. Schröder, U.; Wadhawan, J. D.; Compton, R. G.; Marken, F.; Suarez, P. A.; Consorti, C. S.; de Souza, R. F.; Dupont, J., Water-induced accelerated ion diffusion: voltammetric studies in 1-methyl-3-[2, 6-(S)-dimethylocten-2-yl] imidazolium tetrafluoroborate, 1-butyl-3-methylimidazolium tetrafluoroborate and hexafluorophosphate ionic liquids. *New J. Chem.* **2000,** *24*, 1009–1015.